



# CHORUS

This is the accepted manuscript made available via CHORUS. The article has been published as:

## First-principles simulations of exciton diffusion in organic semiconductors

Xu Zhang, Zi Li, and Gang Lu

Phys. Rev. B **84**, 235208 — Published 22 December 2011

DOI: [10.1103/PhysRevB.84.235208](https://doi.org/10.1103/PhysRevB.84.235208)

# First-principles simulations of exciton diffusion in organic semiconductors

Xu Zhang, Zi Li and Gang Lu

*Department of Physics and Astronomy, California State University Northridge, Northridge, California 91330-8268, USA*

Exciton diffusion is crucial for the performance of organic semiconductors in photovoltaic and solid state lighting applications. We propose a first-principles approach that can predict exciton dynamics in organic semiconductors. The method is based on time-dependent density functional theory to describe energy and many-body wave-functions of excitons. Non-adiabatic *ab initio* molecular dynamics is used to calculate phonon-assisted transition rates between localized exciton states. Using Monte Carlo simulations, we determine exciton diffusion length, lifetime, diffusivity and harvesting efficiency in poly(3-hexylthiophene) (P3HT) polymers at different temperatures, which agree very well with experiments. We find that exciton diffusion is primarily determined by the density of states of low-energy excitons. A widely speculated diffusion mechanism, namely an initial downhill migration followed by thermally activated migration, is confirmed and elucidated by the simulations. Some general guidelines for designing more efficient organic solar cells are obtained from the simulations.

PACS numbers: 72.80.Le, 71.10.Li, 71.15.Pd

## I. INTRODUCTION

Exciton diffusion is of great importance to the performance of organic optoelectronic devices, including organic photovoltaics and solid state lighting. For instance, in organic solar cells high exciton mobility is desirable because excitons have to migrate to the donor/acceptor interfaces for charge separation within their lifetimes.<sup>1</sup> In contrast, in electroluminescent devices such as organic light emitting diodes, efficient exciton diffusion would increase the probability that the excitons reach the quenching sites, contributing to the degradation of the devices performance.<sup>2</sup> Therefore, the ability to control exciton dynamics in organic semiconductors, either by facilitating or hindering exciton diffusion is crucial to the design of the optoelectronic devices. However, such ability hinges upon fundamental understanding of exciton diffusion mechanism. In addition, it is highly desirable to be able to predict exciton diffusion so that promising materials can be identified or pre-screened computationally prior to their synthesis. Here we propose a first-principles approach that can predict exciton dynamics in organic semiconductors and elucidate exciton diffusion mechanism. Such a theoretical tool can greatly expand our capability to rationally design more efficient organic optoelectronic materials.

Earlier theoretical work has employed Forster type energy transfer model to calculate exciton transition rates based on the empirical Miller-Abrahams form;<sup>3,4</sup> these approaches are not material specific and contain empirical parameters, thus have limited predictive power. To be more predictive, quantum chemical methods have been put forward in conjunction with a distributed monopole model to determine the exciton transition rates employing the Fermi golden rule.<sup>5-8</sup> However, all these methods assume a Gaussian distribution of exciton density of states as well as perturbation theories and harmonic approximations, whose validity is not generally established. More importantly, none of the methods above

has considered explicitly the many-body wave-functions and energy levels of the excitons - both are important for exciton dynamics. The proposed approach overcomes these deficiencies and is based on the time-dependent density functional theory (TDDFT)<sup>9</sup> to describe exciton states, including energy levels and many-body wave-functions. The non-adiabatic *ab initio* molecular dynamics (MD)<sup>10,11</sup> is used to determine the phonon-assisted transition rates between localized exciton states. In conjunction with Monte Carlo method, this approach can simulate exciton dynamics in semiconducting polymers at different temperatures.

In this paper, we will study exciton diffusion in conjugate polymer P3HT, which is the donor material in the state-of-the-art bulk heterojunction solar cells, reaching the power conversion efficiency of 5 - 7 %.<sup>12-14</sup> The knowledge gained from this study is expected to be translated to other organic semiconductors as well. In realistic photovoltaic devices - either pure P3HT films or the bulk heterojunctions, there always exist amorphous interphases<sup>15</sup> and interfaces<sup>16</sup>; since exciton diffusion in these amorphous phases limits the overall exciton dynamics, in this paper we will focus on exciton diffusion in amorphous P3HT.

## II. METHODOLOGY

We have developed a theoretical framework that can predict the exciton dynamics including exciton diffusion length, diffusion lifetime, diffusivity and harvesting efficiency from first-principles simulations. The multiscale framework integrates *ab initio* Born-Oppenheimer MD, TDDFT (with range-separated exchange-correlation functional), non-adiabatic *ab initio* MD and Monte Carlo simulations; the coherent integration of the computational components is summarized in the flowchart shown in Fig. 1, which will be elaborated in the following.

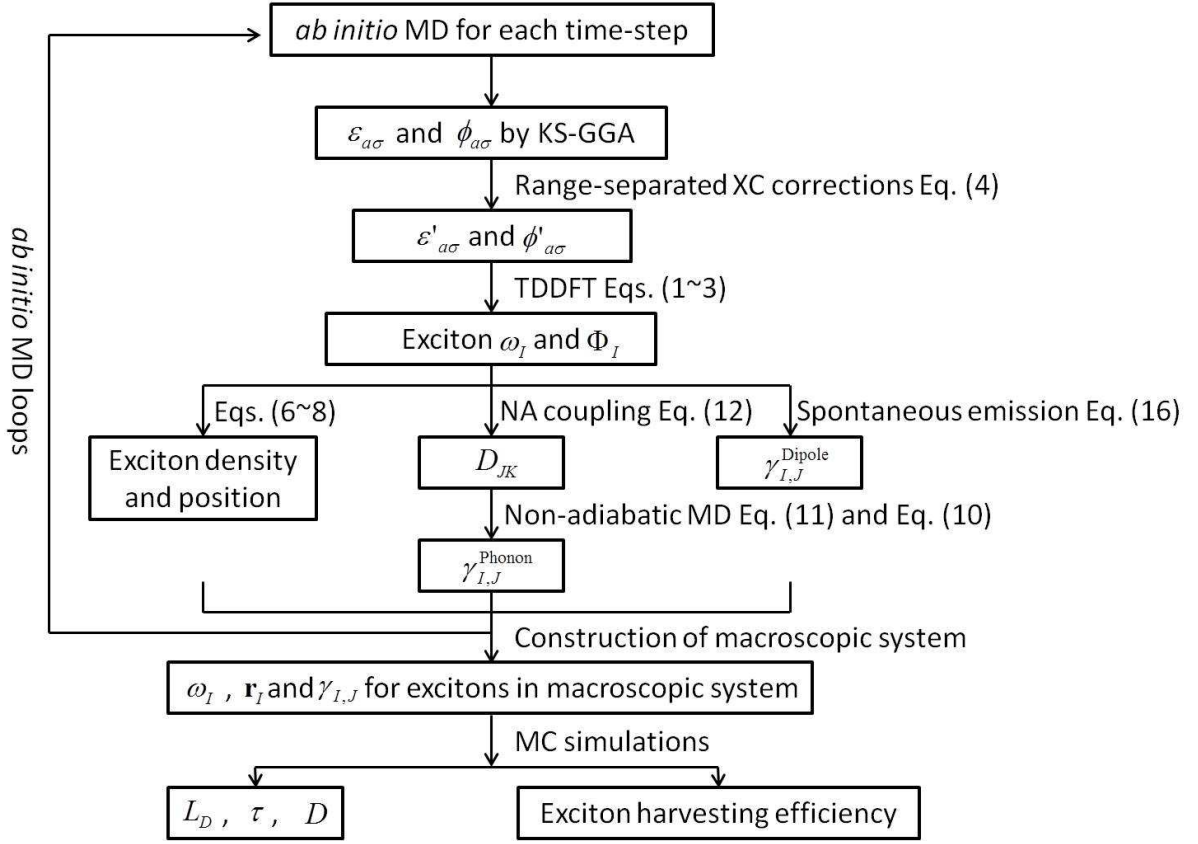


FIG. 1. Flowchart of the multiscale simulation framework.

### A. Determining exciton states

We first carry out *ab initio* MD based on the Kohn-Sham (KS) DFT to capture the effect of static and dynamic disorder on the ground state electronic structure. At each MD time-step, we determine the energy levels and many-body wave-functions of the excitons from the KS eigenvalues  $\epsilon_{i\sigma}$  and eigenfunctions  $\phi_{i\sigma}$  following the TDDFT formulation of Casida<sup>17</sup>. To this end, we solve the following non-Hermitian pseudo-eigenvalue equation at each MD step:

$$\begin{pmatrix} \mathbf{A} & \mathbf{B} \\ \mathbf{B}^* & \mathbf{A}^* \end{pmatrix} \begin{pmatrix} \mathbf{X}_I \\ \mathbf{Y}_I \end{pmatrix} = \omega_I \begin{pmatrix} \mathbf{1} & \mathbf{0} \\ \mathbf{0} & -\mathbf{1} \end{pmatrix} \begin{pmatrix} \mathbf{X}_I \\ \mathbf{Y}_I \end{pmatrix}, \quad (1)$$

where the pseudo-eigenvalue  $\omega_I$  is the  $I$ th exciton energy level; the matrix elements of  $\mathbf{A}$  and  $\mathbf{B}$  in the basis of KS states  $\{ij\sigma\}$  are given by

$$\begin{aligned} A_{ij\sigma,kl\tau} &= \delta_{i,k}\delta_{j,l}\delta_{\sigma,\tau}(\epsilon_{j\sigma} - \epsilon_{i\sigma}) + K_{ij\sigma,kl\tau}, \\ B_{ij\sigma,kl\tau} &= K_{ij\sigma,lk\tau}. \end{aligned} \quad (2)$$

Here  $K$  is the coupling matrix where indices  $i$  and  $k$  indicate the occupied orbitals, and  $j$  and  $l$  represent the virtual orbitals. According to the Assignment Ansatz of Casida, the many-body wave-function of the exciton

state  $I$ ,  $\Phi_I$ , is written as

$$\Phi_I \approx \sum_{ij\sigma} \frac{\mathbf{X}_{I,ij\sigma} + \mathbf{Y}_{I,ij\sigma}}{\sqrt{\omega_I}} \hat{a}_{j\sigma}^\dagger \hat{a}_{i\sigma} \Phi_0, \quad (3)$$

where  $\hat{a}_{i\sigma}$  is the annihilation operator acting on the  $i$ th KS orbital with spin  $\sigma$ , and  $\Phi_0$  is the ground state many-body wave-function taken to be the single Slater determinant (SD) of the occupied KS orbitals.

To describe charge transfer excitations accurately, we incorporate a range-separated exchange-correlation (XC) functional<sup>18,19</sup> into the TDDFT formalism. The range-separated XC functional combines Hartree-Fock (HF) exchange to reproduce  $-1/r$  asymptotic behavior of the exchange potential at a long-range and the Generalized Gradient Approximation (GGA) at a short-range; it has been shown to describe  $\pi \rightarrow \pi^*$  transitions accurately in conjugated polymers<sup>20</sup>. The range-separated functional can be expressed as  $E'_{xc} = E_{xc,GGA} - E_{x,GGA}^{LR} + E_{x,HF}^{LR}$ , where  $E_{xc,GGA}$  is the GGA energy functional,  $E_{x,GGA}^{LR}$  is the long-range part of the GGA exchange energy functional, and  $E_{x,HF}^{LR}$  is the long-range part of Hartree-Fock exchange integral. We have recently proposed an efficient range-separated XC method<sup>21</sup> which is used to correct the KS eigenvalues and eigenfunctions in the TDDFT formalism. These corrections are carried out at each MD

step as indicated in the flowchart Fig. 1. In the following, the superscript prime is denoted for quantities that are corrected by the range-separated XC functional from the GGA results. Indices  $a$  and  $b$  run over occupied orbitals ( $i$ ) and virtual orbitals ( $j$ ). In the basis of KS eigenfunctions  $\phi_{a\sigma}$ , the corrected Hamiltonian matrix elements are:<sup>21</sup>

$$\begin{aligned} \hat{H}'_{ab\sigma} = & \epsilon_{a\sigma}\delta_{ab} - \int \phi_{b\sigma}^*(\mathbf{r})V_{x,\text{GGA}}^{\text{LR},\sigma}[\rho_\sigma(\mathbf{r}),\rho_\tau(\mathbf{r})]\phi_{a\sigma}(\mathbf{r})d\mathbf{r} \\ & - \sum_c^{\text{occ}} [\phi_{b\sigma}^*\phi_{c\sigma} | \frac{\text{erf}(\mu r)}{r} | \phi_{c\sigma}^*\phi_{a\sigma}]. \end{aligned} \quad (4)$$

Here  $V_{x,\text{GGA}}^{\text{LR},\sigma}$  is the long-range part of the GGA exchange potential for spin  $\sigma$ ;  $\rho_\sigma$  is the charge density of spin  $\sigma$  calculated as  $\rho_\sigma(\mathbf{r}) = \sum_c^{\text{occ}} \phi_{c\sigma}^*(\mathbf{r})\phi_{c\sigma}(\mathbf{r})$ , and the Coulomb product  $[f|\frac{1}{r}|g] = \int \int \frac{f(\mathbf{r}_1)g(\mathbf{r}_2)}{|\mathbf{r}_1-\mathbf{r}_2|}d\mathbf{r}_1d\mathbf{r}_2$  has been introduced here.  $\mu$  is the range-separation parameter chosen as  $0.62 \text{ \AA}^{-1}$  which has been well validated<sup>18,21</sup>. The index  $c$  includes all occupied orbitals. The KS eigenvalue  $\epsilon'_{a\sigma}$  and eigenfunction  $\phi'_{a\sigma}$  can be obtained via a direct diagonalization of the Hamiltonian matrix  $\hat{H}'$ , and are used in the TDDFT calculation with Eq. (1). With the corrected eigenvalues and eigenfunctions, the coupling matrix  $K$  is given by

$$\begin{aligned} K_{ij\sigma,kl\tau} = & [\phi'_{i\sigma}^*\phi'_{j\sigma} | \frac{1}{r} | \phi'_{k\tau}\phi'_{l\tau} | - \delta_{\sigma\tau} [\phi'_{i\sigma}^*\phi'_{k\tau} | \frac{\text{erf}(\mu r)}{r} | \phi'_{j\sigma}\phi'_{l\tau} ] \\ & + \int \phi'_{i\sigma}^*(\mathbf{r})\phi'_{j\sigma}(\mathbf{r}) \frac{\delta^2(E_{\text{xc,GGA}} - E_{\text{x,GGA}}^{\text{LR}})}{\delta\rho_\sigma(\mathbf{r})\delta\rho_\tau(\mathbf{r}')} \phi'_{k\tau}(\mathbf{r}')\phi'_{l\tau}(\mathbf{r}')d\mathbf{r}d\mathbf{r}'. \end{aligned} \quad (5)$$

Thus in the calculation of Eq. (2), the eigenvalues  $\epsilon_{i\sigma}$  should be replaced by  $\epsilon'_{i\sigma}$ , with the coupling matrix determined by Eq. (5).

## B. Exciton charge density and spatial positions

Given the many-body wave-functions, one can determine the charge density of the exciton. Here, we consider the spin-restricted case to focus on singlet excitons although the same approach can be generalized to triplet excitons. In an  $N$ -electron system, the density operator is  $\hat{\rho}(\mathbf{r}) = \sum_{n=1}^N \delta(\mathbf{r} - \mathbf{r}_n)$ . Hence the charge density of the  $I$ th excited state can be derived as

$$\begin{aligned} \langle \Phi_I | \hat{\rho}(\mathbf{r}) | \Phi_I \rangle = & \rho_0(\mathbf{r}) + \sum_{i,j,j'} z_{I,ij}^* z_{I,ij'} \phi_j^*(\mathbf{r})\phi_{j'}(\mathbf{r}) \\ & - \sum_{i',j} z_{I,ij}^* z_{I,i'j} \phi_{i'}^*(\mathbf{r})\phi_j(\mathbf{r}), \end{aligned} \quad (6)$$

where  $\rho_0(\mathbf{r}) = \sum_c^{\text{occ}} \phi_c^*(\mathbf{r})\phi_c(\mathbf{r})$  is the charge density of the KS ground state and  $z_{I,ij} = (\mathbf{X}_{I,ij} + \mathbf{Y}_{I,ij})/\sqrt{\omega_I}$ . Since an exciton is a bond state of a quasi-electron and a quasi-hole, the second term on the right hand side of Eq.

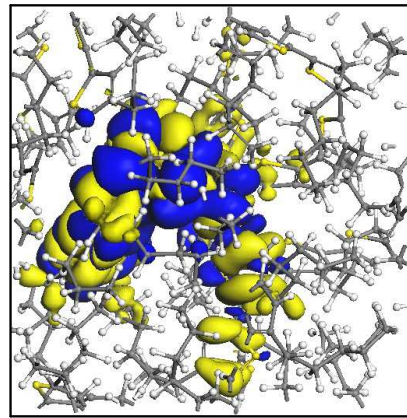


FIG. 2. Charge density of the lowest energy exciton in amorphous P3HT. The computational box is of a dimension of 1.8 nm. The blue (yellow) iso-surface illustrates the charge density distribution at  $\pm 0.005 \text{ \AA}^{-3}$ . The positive (negative) charge density corresponds to the quasi-electron (hole). The gray, white, and yellow spheres denote C, H, and S atoms, respectively.

(6) represents the charge density of the quasi-electron and the third term corresponds to the charge density of the quasi-hole. This identification is consistent with the fact that the index  $i$  refers to the occupied orbitals (holes), while  $j$  refers to the virtual orbitals (electrons) as in Eq. (2). Therefore one can represent the charge density of an exciton by the corresponding densities of its quasi-electron and quasi-hole. This representation is convenient because it reduces the many-body object (the charge density of the exciton) to the single-particle densities, which can be easily visualized and analyzed. For amorphous P3HT, we find that the quasi-electron and quasi-hole are localized on the *same* P3HT chain shown in Fig. 2, consistent with experimental observation of intra-chain Frenkel excitons<sup>22-24</sup>. With increased crystalline order, we find that the excitons acquire both intra- and inter-chain characteristics, also agreeing with experimental observations<sup>24</sup>. In addition, we estimate that the first excitation energy of the crystalline P3HT ranges from 1.5 eV to 2.4 eV, comparing well to the corresponding experimental value of  $\sim 2.0 \text{ eV}$ <sup>25</sup>. For the crystalline P3HT, we find that the first excitation energy depends sensitively on the stacking order of  $\pi - \pi$  wave-functions, and the two numbers cited above correspond to two opposite stacking orders. Overall, the TDDFT calculations provide an accurate description of the static properties of excitons in P3HT.

To simulate exciton diffusion, it is often useful to define spatial positions of the excitons. With the position operator  $\hat{\mathbf{r}} = \sum_{n=1}^N \mathbf{r}_n$ , the position of the exciton  $I$  in

the  $N$ -electron system is given by

$$\begin{aligned} \langle \Phi_I | \hat{\mathbf{r}} | \Phi_I \rangle &= \int \rho_0(\mathbf{r}) \mathbf{r} d\mathbf{r} + \sum_{i,j,j'} z_{I,ij}^* z_{I,ij'} \langle \phi_j | \mathbf{r} | \phi_{j'} \rangle \\ &- \sum_{i',j} z_{I,ij}^* z_{I,i'j} \langle \phi_{i'} | \mathbf{r} | \phi_i \rangle. \end{aligned} \quad (7)$$

On the right hand side of Eq. (7), the first term is the sum of all electron positions in the ground state; the second (third) term corresponds to the position of the quasi-electron  $\mathbf{r}_e$  (quasi-hole  $\mathbf{r}_h$ ). We can thus define the position of the exciton  $I$   $\mathbf{r}_{ex}$  as

$$\mathbf{r}_{ex} = \frac{\mathbf{r}_e + \mathbf{r}_h}{2}. \quad (8)$$

Again the advantage of this definition is to relate the many-body quantity of the exciton position with single-particle quantities ( $\mathbf{r}_e$  and  $\mathbf{r}_h$ ).

### C. Exciton transition rates

Next, we determine phonon-assisted transition rates and the spontaneous emission rates of the excitons. We attribute exciton diffusion to the phonon-assisted transitions, including adiabatic evolution of the excited states and the non-adiabatic hopping between the excited states. The thermal fluctuations of the ions could lead to overlap between the exciton states in space and energy, and thus promote exciton transitions between the localized exciton states. Since these transitions can be non-adiabatic, the non-adiabatic *ab initio* molecular dynamics is used to describe the phonon-assisted transitions. During a molecular dynamics trajectory, the time-dependent many-body wave-function of the exciton state,  $\Psi(t)$ , can be expanded by a linear combination of a complete basis set consisting of the adiabatic ground state and the excited states  $\Phi_I(\mathbf{R}(t))$  at the present ionic positions  $\mathbf{R}(t)$ :

$$\Psi(t) = \sum_{I=0}^{\infty} C_I(t) \Phi_I(\mathbf{R}(t)), \quad (9)$$

where  $C_I(t)$  is the expansion coefficient. Let the exciton start in a pure state  $I$  at  $t = 0$ , i.e.,  $\Psi(0) = \Phi_I(\mathbf{R}(0))$ ; then the coefficient  $C_J(t)$  in Eq. (9) can be labeled as  $C_J^{(I)}(t)$  with the initial condition that  $C_J^{(I)}(0) = \delta_{I,J}$ . At  $t > 0$ , ions move and  $\Psi(t)$  becomes a mixed state. Therefore  $|C_J^{(I)}(t)|^2$  represents the probability that the exciton makes a transition from the state  $I$  to the state  $J$  during a small time interval of  $\delta t$  (in this case  $\delta t = t - 0$ ). The phonon-assisted exciton transition rate from the state  $I$  to  $J$ ,  $\gamma_{I,J}^{\text{Phonon}}$  is thus given by

$$\gamma_{I,J}^{\text{Phonon}} = \left\langle \frac{|C_J^{(I)}(t)|^2}{t} \right\rangle_{\delta t}. \quad (10)$$

The average is taken over a short MD trajectory of  $\delta t$ . Here, we use  $\delta t = 100$  fs to determine the phonon-assisted transition rates. The evolution of  $C_J^{(I)}(t)$  can be determined on-the-fly from the non-adiabatic *ab initio* molecular dynamics. Substituting Eq. (9) into the time-dependent Schrodinger equation, one arrives at the following equation involving the expansion coefficient  $C_J(t)$ :

$$\frac{\partial}{\partial t} C_J(t) = - \sum_K C_K(t) \left( \frac{i}{\hbar} \omega_K \delta_{JK} + D_{JK} \right). \quad (11)$$

A standard second-order finite-difference method with a time-step of  $10^{-3}$  fs is employed to propagate the coefficient  $C_J(t)$ . And  $D_{JK}$  is the non-adiabatic coupling between two many-body electronic states  $J$  and  $K$ ,

$$D_{JK} \equiv \langle \Phi_J | \nabla_{\mathbf{R}} | \Phi_K \rangle \cdot \frac{d\mathbf{R}}{dt} = \langle \Phi_J | \frac{\partial}{\partial t} | \Phi_K \rangle. \quad (12)$$

Substituting Eq. (3) into Eq. (12), we can obtain  $D_{JK}$  as

$$\begin{aligned} D_{JK} &= \sum_{ii'jj'} z_{J,ij}^* z_{K,i'j'} \langle \Phi_{ij} | \frac{\partial}{\partial t} | \Phi_{i'j'} \rangle \\ &= \sum_{i,j \neq j'} z_{J,ij}^* z_{K,ij'} d_{jj'} - \sum_{i \neq i',j} z_{J,ij}^* z_{K,i'j} d_{i'i}, \end{aligned} \quad (13)$$

where  $\Phi_{ij} = \hat{a}_j^\dagger \hat{a}_i \Phi_0$  is a single SD of the KS orbitals, promoting an electron from an occupied state  $i$  to a virtual state  $j$ .  $d_{jk} = \langle \phi_j | \frac{\partial}{\partial t} | \phi_k \rangle$  is the non-adiabatic coupling between the KS orbitals. One can show that

$$\langle \Phi_{ij} | \frac{\partial}{\partial t} | \Phi_{i'j'} \rangle = \begin{cases} 0, & \text{if } i = i' \text{ and } j = j', \\ d_{jj'}, & \text{if } i = i' \text{ and } j \neq j', \\ 0, & \text{if } i \neq i' \text{ and } j \neq j', \\ -d_{i'i}, & \text{if } i \neq i' \text{ and } j = j', \end{cases} \quad (14)$$

where  $d_{ii} = 0$  has been used. Hence  $\langle \Phi_{ij} | \frac{\partial}{\partial t} | \Phi_0 \rangle = d_{ji}$ , and the non-adiabatic coupling between the exciton state  $J$  and the ground state is obtained as

$$D_{J0} = \sum_{i,j} z_{J,ij}^* d_{ji}. \quad (15)$$

Although the non-adiabatic coupling between the ground state and the excited states  $D_{J0}$  can be rigorously determined by TDDFT<sup>26</sup>, there is no such rigorous formulation for the non-adiabatic coupling between the excited states, therefore approximate many-body wave-functions in Eq. (3) have to be used in calculating Eq. (12).

Excitons can decay from a higher energy to a lower energy or even to the ground state (i.e., exciton annihilation) through the so-called spontaneous emission mechanism. Based on the transition dipole moment approximation, we can estimate the spontaneous emission rate between two exciton states as

$$\gamma_{I,J}^{\text{Dipole}} = \frac{4n(\omega_I - \omega_J)^3 |\langle \Phi_I | \hat{\mathbf{r}} | \Phi_J \rangle|^2}{3c^3}, \quad (16)$$

where  $c$  is the vacuum speed of light and  $n$  is the refractive index which takes a value of 1.5 for P3HT<sup>27</sup>. Similar to Eq. (7), the transition dipole moment can be evaluated as

$$\begin{aligned} \langle \Phi_I | \hat{\mathbf{r}} | \Phi_J \rangle &= \sum_{i,j,j'} z_{I,ij}^* z_{J,ij'} \langle \phi_j | \mathbf{r} | \phi_{j'} \rangle \\ &- \sum_{i,i',j} z_{I,ij}^* z_{J,i'j} \langle \phi_{i'} | \mathbf{r} | \phi_i \rangle, \end{aligned} \quad (17)$$

where  $I$  and  $J$  are the exciton states, and

$$\langle \Phi_I | \hat{\mathbf{r}} | \Phi_0 \rangle = \sum_{i,j} z_{I,ij}^* \langle \phi_j | \mathbf{r} | \phi_i \rangle, \quad (18)$$

represents the dipole moment between the exciton state  $I$  and the ground state.

Although the spontaneous emission contributes only to the energy downhill transitions, the phonon-assisted transitions could take place both downhill and uphill. To ensure detailed balance, the thermal equilibrium transition rate  $\gamma_{I,J}$  can be defined as<sup>28</sup>

$$\gamma_{I,J} = \begin{cases} \gamma_{I,J}^{\text{Phonon}} \exp\left(-\frac{\omega_J - \omega_I}{k_B T}\right), & \text{if } \omega_J \geq \omega_I, \\ \gamma_{I,J}^{\text{Phonon}} + \gamma_{I,J}^{\text{Dipole}}, & \text{if } \omega_J < \omega_I, \end{cases} \quad (19)$$

where  $k_B$  is the Boltzmann constant and  $T$  is temperature.

#### D. Construction of macroscopic system and Monte Carlo simulations

To examine exciton diffusion in a length-scale that is relevant to experiments, we divide the entire ‘‘macroscopic’’ system of interest into  $L_x \times L_y \times L_z$  cubes; each cube should be chosen as large as computationally feasible, but at minimum the cube should accommodate the localized wave-functions of the quasi-electron and the quasi-hole. The *ab initio* MD simulation is carried out for one of the cubes, termed home cube; the KS energy and wave-functions obtained along the MD trajectories are used to construct the electronic states of the macroscopic system approximately. More specifically, to model an amorphous structure, the KS orbitals are randomly selected and rotated from the MD snap-shots of the home cube before placing them into the other cubes. In the same vein, we can model a crystalline structure by letting the KS orbitals be the same in each cube (the polymer chains in each cube can be either warped or straight). Moreover, we can also generate a lamellar structure by keeping the KS orbitals the same in one dimension. In each case, the KS orbitals are used to determine the exciton positions  $\mathbf{r}_I$  following Eq. (7) and (8) in the macroscopic system. The transition rates within each cube (or intra-cube transition rates) are calculated by Eq. (19) while the inter-cube transition rates are determined by

the distance between the excitons and the relevant intra-cube transition rates. The rationale behind this approximation and the detailed procedure can be found in Ref. 29 and 30. In this manner, the energies  $\omega_I$ , positions  $\mathbf{r}_I$ , and transition rates  $\gamma_{I,J}$  for each excitons in the macroscopic system can be obtained.

Exciton diffusion is modeled as random walks using Monte Carlo (MC) simulations. For diffusion of the exciton  $I$ , one can generate an event table with  $M + 1$  transition probabilities ( $M$  is the number of excitons considered in the simulation): transition probabilities from the exciton  $I$  to  $M - 1$  neighboring excitons,  $P_{1,2,\dots,M-1} = \gamma_{I,J} \times \Delta t$  with  $J = 1, \dots, I - 1, I + 1, \dots, M$ ; annihilation probability,  $P_M = \gamma_{I,0} \times \Delta t$ ; and the probability to remain at the same state  $I$ ,  $P_{M+1} = 1 - (P_1 + P_2 + \dots + P_M)$ .  $\Delta t$  is the time-step of the MC simulations. With these probabilities, a diffusion trajectory of the exciton  $I$  is obtained by executing MC moves until the exciton is annihilated. From the trajectory, one can determine the lifetime  $t$  (the number of MC moves multiplied by  $\Delta t$ ) and the maximum distance  $d_{\text{max}}$  of exciton diffusion for each trajectory. Averaging over all trajectories with the same initial exciton position gives the exciton diffusion length, lifetime, and diffusivity by  $L_D = \langle d_{\text{max}} \rangle$ ,  $\tau = \langle t \rangle$ , and  $D = \langle d_{\text{max}}^2 \rangle / \tau$ , respectively where the brackets indicate the average. The exciton harvesting efficiency can also be determined from these relevant trajectories as shown in Sec. III B. One can then repeat the same procedure for different excitons.

### III. APPLICATION TO CONJUGATED POLYMER P3HT

#### A. Computational details

*Ab initio* Born-Oppenheimer molecular dynamics is carried out for the home cube (shown in Fig. 2) of a dimension of 1.8 nm with periodic boundary conditions. The supercell contains 606 atoms, including three P3HT chains each with eight thiophene rings, leading to a mass density of 1.1 g/cm<sup>3</sup>, which is similar to the experimental value. The initial structure of the P3HT chains, starting from a randomly placed and warped configuration, is fully relaxed to reach the local energy minimum. The system is brought to a desired temperature by MD with a repeated velocity scaling, and is then kept at the desired temperature for 500 fs with 1 fs time-step to reach the thermal equilibrium. Finally, the micro-canonical production MD run is carried out for 1000 fs with 1 fs time-step for each temperature. We have confirmed that the simulated system is equilibrated during the micro-canonical MD run<sup>29</sup>. The PAW pseudopotentials<sup>31</sup> and Perdew-Burke-Ernzerhof (PBE) functional<sup>32</sup> as implemented in the VASP package<sup>33,34</sup> are used in the *ab initio* calculations performed at  $\Gamma$  point with 300 eV energy cutoff. Six highest occupied KS orbitals and nine lowest unoccupied KS orbitals are included in the Casida’s for-

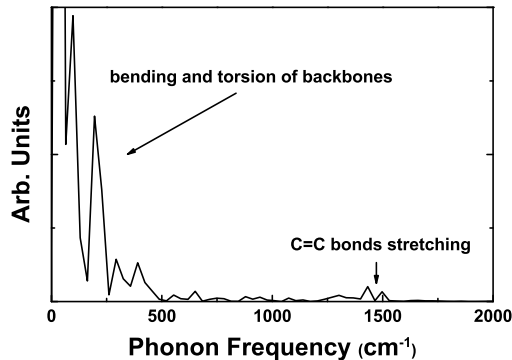


FIG. 3. The Fourier transform of the lowest exciton energy level at 300 K. The frequencies of the bending and torsion modes of the backbones are below  $500 \text{ cm}^{-1}$ , and the stretching frequency of C=C bonds is about  $1500 \text{ cm}^{-1}$ .

mulation to produce 54 exciton states. In each MD step, we obtain the KS energies and orbitals which are then used to calculate the many-body wave-functions and the energies of the 54 excitons.

The entire system of interest consists of  $30 \times 30 \times 30$  cubes for which the Monte Carlo simulations are carried out (the dimensions of the simulated system are much larger than the diffusion length, thus are sufficient to represent the realistic macroscopic system). By using different random number sequences, we have constructed 100 different configurations of the entire system. And for each configuration, 100 trajectories of exciton diffusion are modeled by Monte Carlo. In total, we have generated  $10^4$  trajectories for each initial exciton states considered in the present work. The time-step  $\Delta t$  in the Monte Carlo simulations should be chosen judiciously so that  $\sum_{m=1}^M P_m < 1$  and the minimal time-step should be greater than or equal to 1 fs, which is the time-step of the MD simulations. We have performed Monte Carlo simulations using  $\Delta t = 1$  fs and 10 fs, respectively, and obtained the similar results for the diffusion length and lifetime.

## B. Results and discussions

The exciton diffusion consists of inter-state transitions (the transitions between two excited states) and annihilations (transitions to the ground state); these transitions can be phonon-assisted or spontaneous. We find that at 300 K the phonon-assisted transition rates range from  $10^8 \text{ s}^{-1}$  to  $10^{13} \text{ s}^{-1}$  and from  $10^6 \text{ s}^{-1}$  to  $10^9 \text{ s}^{-1}$  for the inter-state transitions and annihilations, respectively. The spontaneous emission rates span from 0 to  $10^8 \text{ s}^{-1}$  and from  $10^5 \text{ s}^{-1}$  to  $10^9 \text{ s}^{-1}$  for the inter-state transitions and annihilations, respectively. Thus the inter-state transitions are dominated by the phonon-assisted processes,

TABLE I. Simulated diffusion length  $L_D$  (nm), lifetime  $\tau$  (ns), and diffusivity  $D$  ( $10^{-8} \text{ m}^2/\text{s}$ ) for S1, S2, and S3 excitons at 100 K, 200 K, and 300K, respectively.

	300K			200K			100K		
	S1	S2	S3	S1	S2	S3	S1	S2	S3
$L_D$	5.1	6.4	7.7	2.9	4.4	6.2	1.7	4.2	6.1
$\tau$	2.3	2.4	2.3	1.8	1.6	1.6	3.6	3.6	3.5
$D$	1.5	2.1	3.0	0.6	1.4	2.8	0.1	0.6	1.2

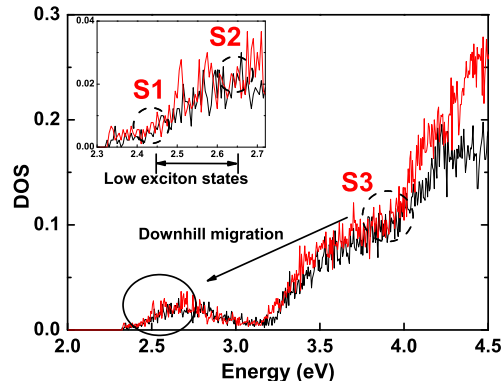


FIG. 4. The exciton density of states for 54 excitons (black curve) and 144 excitons (red curve) in each cube at 300 K. Dashed circles show the energy range of S1, S2, and S3 excitons. Inset: a blown-up view of DOS in the energy range indicated by the solid black circle.

while the phonon-assisted and spontaneous transitions contribute equally to the annihilations. From the Fourier transform of the time-dependent exciton energy levels, we can identify the relevant phonon modes that give rise to the exciton-phonon coupling and the non-adiabatic exciton transitions. As shown in Fig. 3, a number of low frequency phonons arising from the bending and torsion modes of the backbones and a much higher frequency phonon from the stretching mode of C=C bonds are responsible for the phonon-assisted exciton dynamics. These results are in excellent agreement with the experimental observations<sup>35,36</sup>.

In the following, we discuss the simulation results of exciton diffusion in amorphous P3HT. Three representative excitons whose initial energies are labeled by S1, S2 and S3 in the Fig. 4 are considered. Here the density of states (DOS) counts all possible exciton states at a given energy corresponding to all atomic configurations over the course of MD. S1 is at the low-energy tail of the exciton DOS; S2 is 0.2 eV higher than S1 while S3 is 1.5 eV higher than S1. While the energy of S1 and S2 corresponds to the efficient photon adsorption frequencies, the energy of S3 approaches the higher-limit of the solar spectrum. The results of  $L_D$ ,  $\tau$ , and  $D$  from the Monte Carlo simulations are summarized in Table I. The experimental

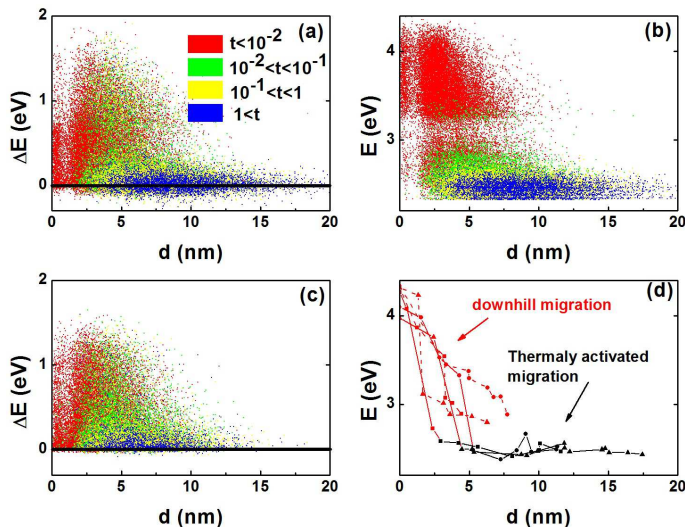


FIG. 5. The energy evolution of S3 exciton vs. diffusion distance from  $10^4$  trajectories. (a) and (c): The exciton energy difference between two adjacent diffusion moves vs. diffusion distance at 300 K (a) and 100 K (c). The color-coding represents different time-ranges; the time is given in ns. (b) The exciton energy vs. the diffusion distance at 300 K. (d) The exciton energy vs. diffusion distance for three randomly selected trajectories at 300 K (solid curves) and 100 K (dash curves). The downhill and thermally activated migration processes are represented by the red and black curves, respectively.

values of exciton diffusion length in P3HT at room temperature scatter considerably: from  $2.6 \sim 5.3 \text{ nm}^{37}$ ,  $4 \text{ nm}^{38}$ ,  $8.5 \text{ nm}^{39}$ , to  $27 \pm 12 \text{ nm}^{40}$ . The corresponding diffusivity ranges from  $5 \times 10^{-8} \text{ m}^2/\text{s}^{38}$ ,  $2 \times 10^{-7} \text{ m}^2/\text{s}^{39}$ , to  $1 \times 10^{-6} \text{ m}^2/\text{s}^{40}$ . To understand the large variation of the experimental values, we also consider a crystalline P3HT structure in the Monte Carlo simulations and determine  $L_D$ ,  $\tau$ , and  $D$  as  $17.2 \text{ nm}$ ,  $0.35 \text{ ns}$ , and  $9 \times 10^{-7} \text{ m}^2/\text{s}$ , respectively. Clearly the diffusion length and diffusivity in the crystalline P3HT are much higher than those of the amorphous P3HT, and in fact the results are in line with the largest experimental values. Therefore, the exciton dynamics depends sensitively on the structural order of the polymer - more than two orders of magnitude increase in diffusivity can be achieved by improving the structural order. Additionally, the calculated exciton lifetime is  $\sim 1 \text{ ns}$ , compatible to the experimental values that range from a few hundred ps to  $\sim 1 \text{ ns}^{41}$ . Finally, it is evident from Table I that the diffusion length and diffusivity increase with the temperature and the exciton with a higher energy has a greater diffusion length and diffusivity.

It has been speculated that exciton diffusion in conjugated polymers is governed by two processes: an initial downhill migration towards lower energies followed by a thermally activated migration<sup>2,41,42</sup>. However, there is no direct evidence that such processes exist and the general behavior of the diffusion processes remains to be

understood. Our simulations have unambiguously confirmed that such processes indeed exist and provided a fundamental understanding of the processes. In Fig. 5, we display the evolution of exciton energy vs. diffusion distance for  $10^4$  trajectories. Each data point corresponds to an MC move with increasing diffusion distance; a positive (negative)  $\Delta E$  in Fig. 5(a) and (c) corresponds to an energy loss (gain). Therefore the initial downhill migration is represented by the red color with positive  $\Delta E$ , while the thermally activated migration is represented by the yellow and blue colors with oscillating  $\Delta E$  across the zero energy. The initial downhill migration completes within  $10^{-2} \text{ ns}$ , much faster than the thermally activated migration ( $\sim 1 \text{ ns}$ ). Shown in Fig. 5(b), the downhill process is characterized by a smaller diffusion distance ( $\sim 5 \text{ nm}$ ) but with a greater energy loss ( $> 1 \text{ eV}$ ); in contrast the thermally activated process contributes to a much longer diffusion distance (up to  $20 \text{ nm}$ ) but with a much smaller energy variation ( $\sim 0.2 \text{ eV}$ ). It can also be observed from Fig. 5(b) that the thermally activated process involves exclusively the low-energy excitons (i.e., the width of the blue strip is  $0.2 \text{ eV}$ ); these low-energy exciton states are also indicated in Fig. 4. By comparing Fig. 5(a) and (c), one finds that the thermally activated migration is suppressed at 100 K - there is an absence of energy gain or negative  $\Delta E$  in Fig. 5(c).

Next, we examine the general behavior of exciton diffusion by focusing on the three representative excitons. Fig. 6 shows the percentage distribution of the diffusion distance obtained from  $10^4$  diffusion trajectories at different temperatures. From Fig. 6 and Table I, we find that (i) the diffusion length increases with temperature for all three excitons, particularly for the low-energy excitons such as S1; (ii) the diffusion behavior of the higher energy excitons (such as S2 and S3) is similar at 300 K. These two observations can be understood from the diffusion mechanism outlined above. Since exciton diffusion in real space corresponds to transitions between excited states in energy space, a lower exciton DOS implies fewer possible states for a migrating exciton to make transitions to, hence the diffusion is suppressed. This is the case for S1 exciton - the DOS of S1 is very small and so is its diffusion length at 100 K. At a higher temperature, however, S1 exciton can gain its energy from the phonons promoting S1 to a higher energy state with a greater DOS. Hence the diffusion of S1 is enhanced by increasing temperature. In contrast, S3 can lower its energy via the downhill migration to S2. Since the diffusion distance is primarily determined by the thermally activated process, S3 has a slightly larger diffusion distance than S2 (their difference stems from the prior downhill migration from S3 to S2). Consequently there exists an optimal excitation energy,  $E_{\text{opt}}$  which is approximately  $0.2 \text{ eV}$ . The energy of S2 is optimal for diffusion; below S2, exciton diffusion at low temperatures is minimal because it has to acquire enough thermal energy for a considerable diffusion distance. On the other hand, a much higher exciton

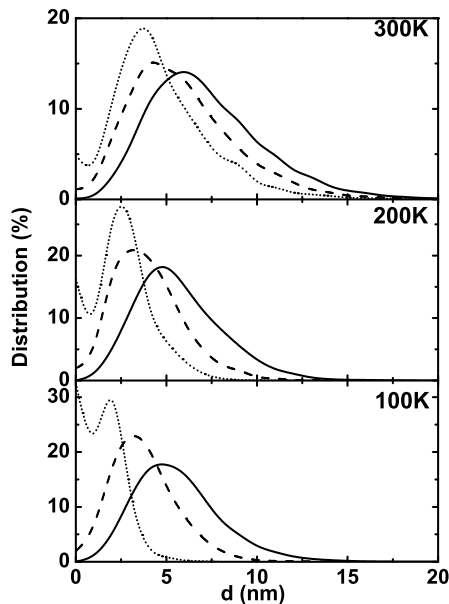


FIG. 6. Statistics (percentage) of exciton diffusion distance for  $10^4$  exciton diffusion trajectories at 100 K, 200 K, and 300 K. Solid, dashed, and dotted curves correspond to S3, S2, and S1 exciton, respectively.

energy does not lead to a much longer diffusion distance because the extra energy will be “lost” to the phonons via inefficient downhill migration.

The diffusion distance distribution shown in Fig. 6 is also useful to estimate exciton harvesting efficiency - an important quantity for photovoltaic performance. For a given diffusion distance  $r$ , the integration of the distribution percentage from  $r$  to  $\infty$  represents the probability  $p(r)$  that an exciton can be harvested. Consider a planar heterojunction in which P3HT donor layer is sandwiched between two acceptors. Let exciton be formed at distance  $r$  from the interface and assume the excitons are generated homogeneously in the P3HT layer. The harvesting efficiency can be estimated as  $\int_0^L p(r)dr/L$ , where  $L$  is the thickness of the P3HT layer. At 300 K for S3 exciton, we find that the exciton harvesting efficiency as 90%, 70% and 10% for  $L = 6$  nm, 10 nm and 70 nm respectively. In particular, the estimated efficiency of 70% is very close to the experimentally measured photoluminescence quenching efficiency of 68% for P3HT with the same thickness<sup>43</sup>; the corresponding efficiency for S2 exciton is 62%, slightly smaller than the experimental value.

Finally, to verify that 54 excitons in each cube is sufficient to simulate the exciton diffusion in P3HT, we have considered 144 excitons per cube in the simulations - twelve highest occupied KS orbitals and twelve lowest unoccupied KS orbitals in Casida’s formulation. The values for the diffusion length and diffusivity are practically the same as in the case of 54 excitons. This agreement can

be understood from two facts: (1) the DOS below S3 is essentially the same for the two cases as shown in Fig. 4 and (2) the DOS above S3 is irrelevant to the diffusion. The reason behind the second fact is that the diffusion of S3 exciton proceeds with the downhill migration *initially* as shown in Fig. 5(b), which lows its energy towards S2. The states above S3 are not accessed in the diffusion. On the other hand, the energy of S1 and S2 excitons is too low to be thermally elevated above S3. Therefore 54 excitons per cube are sufficient for the diffusion of the three excitons considered here. In general, the number of excitons in each cube should be determined by ensuring that the DOS below the highest relevant exciton state is correctly reproduced.

#### IV. CONCLUSION

To conclude, we have developed a computational capability that could potentially guide rational design of organic optoelectronic materials by predicting exciton dynamics. The theoretical approach is based on first-principles simulations without empirical input. We have studied exciton diffusion in both crystalline and amorphous P3HT conjugated polymers at different temperatures and obtained excellent agreements (including exciton diffusion length, diffusivity, lifetime and harvesting efficiency) with the experimental results. The simulations unambiguously establish the exciton diffusion mechanism and shed light into the exciton diffusion processes that are difficult to obtain by experiments alone. In addition, the simulations provide following guidelines that could be potentially useful in materials design: (1) From a structure perspective, exciton diffusion depends sensitively on the crystalline order - a higher structural order renders a greater diffusion length. More than two orders of magnitude increase in diffusivity can be achieved by optimizing the material structure. (2) From a materials perspective, exciton diffusion depends critically on the electronic density of states near the valence band maximum and conduction band minimum of the semiconductor - a higher density of states near the band edges leads to more low-energy exciton states, yielding a greater diffusion length. The optical gap on the other hand does not play a role in exciton diffusion. (3) There is an optimal photon frequency for exciton diffusion in each material; therefore in designing tandem solar cells, one should consider frequency-dependence both in terms of light adsorption and exciton diffusion in each material to gain the highest overall quantum efficiency.

#### ACKNOWLEDGMENTS

This work was supported by NSF Solar energy grant DMR-1035480 and NSF MRI-R<sup>2</sup> grant DMR-0958596 for computational facility. We acknowledge discussions with Gui Bazan, Carlos Garcia-Cervera and Thuc-Quyen

Nguyen.

- 
- <sup>1</sup> A. C. Mayer, S. R. Scully, B. E. Hardin, M. W. Rowell, and M. D. McGehee, *Mater. Today* **10**, 28 (2007).
  - <sup>2</sup> F. B. Dias, K. T. Kamtekar, T. Cazati, G. Williams, M. R. Bryce, and A. P. Monkman, *Chem. Phys. Chem* **10**, 2096 (2009).
  - <sup>3</sup> S. C. J. Meskers, J. Hubner, M. Oestreich, and H. Bassler, *J. Phys. Chem. B* **105**, 9139 (2001).
  - <sup>4</sup> C. Madigan, and V. Bulovic, *Phys. Rev. Lett* **96**, 046404 (2006).
  - <sup>5</sup> E. Hennebicq, G. Pourtois, G. D. Scholes, L. M. Herz, D. M. Russell, C. Silva, S. Setayesh, A. C. Grimsdale, K. Mullen, J. L. Bredas, and D. Beljonne, *J. Am. Chem. Soc* **127**, 4744 (2005).
  - <sup>6</sup> B. Van Averbeke, and D. Beljonne, *Chem. Phys. Chem* **10**, 3061 (2009).
  - <sup>7</sup> M. E. Kose, P. Graf, N. Kopidakis, S. E. Shaheen, K. Kim, and G. Rumbles, *Chem. Phys. Chem* **10**, 3285 (2009).
  - <sup>8</sup> S. Athanasopoulos, E. Hennebicq, D. Beljonne, and A. B. Walker, *J. Phys. Chem. C* **112**, 11532 (2008).
  - <sup>9</sup> G. Onida, L. Reining, and A. Rubio, *Rev. Mod. Phys.* **74**, 601 (2002).
  - <sup>10</sup> W. R. Duncan, W. M. Stier, and O. V. Prezhdo, *J. Am. Chem. Soc.* **127**, 7941 (2005).
  - <sup>11</sup> C. F. Craig, W. R. Duncan, and O. V. Prezhdo, *Phys. Rev. Lett.* **95**, 163001 (2005).
  - <sup>12</sup> G. Li, V. Shrotriya, J. S. Huang, Y. Yao, T. Moriarty, K. Emery, and Y. Yang, *Nature Mater.* **4**, 864 (2005).
  - <sup>13</sup> Y. Kim, S. Cook, S. M. Tuladhar, S. A. Choulis, J. Nelson, J. R. Durrant, D. D. C. Bradley, M. Giles, I. McCulloch, C. Ha, and M. Ree, *Nature Mater.* **5**, 197 (2006).
  - <sup>14</sup> J. Yang, R. Zhu, Z. Hong, Y. He, A. Kumar, Y. Li, and Y. Yang, *Adv. Mater.* **23**, 3465 (2011).
  - <sup>15</sup> M. Brinkmann, and J. C. Wittmann, *Adv. Mater.* **18**, 860 (2006).
  - <sup>16</sup> A. J. Moule, and K. Meerholz, *Adv. Mater.* **20**, 240 (2008).
  - <sup>17</sup> M. E. Casida, *Recent Advances in Density Functional Methods*, eds Chong DP, pp 155-192, (World Scientific, Singapore, 1995).
  - <sup>18</sup> H. Iikura, T. Tsuneda, T. Yanai, and K. Hirao, *J. Chem. Phys.* **115**, 3540 (2001).
  - <sup>19</sup> Y. Tawada, T. Tsuneda, S. Yanagisawa, T. Yanai, and K. Hirao, *J. Chem. Phys.* **120**, 8425 (2004).
  - <sup>20</sup> A. Karolewski, T. Stein, R. Baer, and S. Kummel, *J. Chem. Phys.* **134**, 151101 (2011).
  - <sup>21</sup> X. Zhang, Z. Li, and G. Lu. Submitted.
  - <sup>22</sup> L. M. Blinov, S. P. Palto, G. Ruani, C. Taliani, A. A. Tevosov, S. G. Yudin, and R. Zamboni, *Chem. Phys. Lett.* **232**, 401 (1995).
  - <sup>23</sup> P. W. M. Blom, V. D. Mihailetschi, L. J. A. Koster, and D. E. Markov, *Adv. Mater.* **19**, 1551 (2007).
  - <sup>24</sup> P. J. Brown, D. S. Thomas, A. Kohler, J. S. Wilson, J. Kim, C. M. Ramsdale, H. Sirringhaus, and R. H. Friend, *Phys. Rev. B* **67**, 064203 (2003).
  - <sup>25</sup> T. Liu, and A. Troisi, *J. Phys. Chem. C* **115**, 2406 (2011).
  - <sup>26</sup> C. Hu, H. Hirai, and O. Sugino, *J. Chem. Phys.* **127**, 064103 (2007).
  - <sup>27</sup> A. J. Morfa, T. M. Barnes, A. J. Ferguson, D. H. Levi, G. Rumbles, K. L. Rowlen, J. van de Lagemaat, *J. Polym. Sci. Pt. B-Polym. Phys.* **49**, 186 (2011).
  - <sup>28</sup> P. V. Parandekar, and J. C. Tully, *J. Chem. Phys.* **122**, 094102 (2005).
  - <sup>29</sup> X. Zhang, Z. Li, and G. Lu, *Phys. Rev. B* **82**, 205210 (2010).
  - <sup>30</sup> N. Vukmirovic, and L. W. Wang, *Nano Lett.* **9**, 3996 (2009).
  - <sup>31</sup> P. E. Blochl, *Phys. Rev. B* **50**, 17953 (1994).
  - <sup>32</sup> J. P. Perdew, K. Burke, and M. Ernzerhof, *Phys. Rev. Lett.* **77**, 3865 (1996).
  - <sup>33</sup> G. Kresse, and J. Hafner, *Phys. Rev. B* **47**, 558 (1993).
  - <sup>34</sup> G. Kresse, and J. Furthmuller, *Phys. Rev. B* **54**, 11169 (1996).
  - <sup>35</sup> N. P. Wells, and D. A. Blank, *Phys. Rev. Lett.* **100**, 086403 (2008).
  - <sup>36</sup> N. Banerji, S. Cowan, E. Vauthey, and A. J. Heeger, *J. Phys. Chem. C* **115**, 9726 (2011).
  - <sup>37</sup> J. E. Kroeze, T. J. Savenije, M. J. W. Vermeulen, and J. M. Warman, *J. Phys. Chem. B* **107**, 7696 (2003).
  - <sup>38</sup> L. Luer, H. J. Egelhaaf, D. Oelkrug, G. Cerullo, G. Lanzani, B. H. Huisman, and D. de Leeuw, *Org. Electron.* **5**, 83 (2004).
  - <sup>39</sup> P. E. Shaw, A. Ruseckas, and I. D. W. Samuel, *Adv. Mater.* **20**, 3516 (2008).
  - <sup>40</sup> S. Cook, L. Han, A. Furube, and R. Katoh, *J. Phys. Chem. C* **114**, 10962 (2010).
  - <sup>41</sup> I. G. Scheblykin, A. Yartsev, T. Pullerits, V. Gulbinas, and V. Sundstrom, *J. Phys. Chem. B* **111**, 6303 (2007).
  - <sup>42</sup> O. V. Mikhnenko, F. Cordella, A. B. Sieval, J. C. Hummelen, P. W. M. Blom, and M. A. Loi, *J. Phys. Chem. B* **112**, 11601 (2008).
  - <sup>43</sup> K. M. Coakley, Y. Liu, M. D. McGehee, K. L. Frindell, and G. D. Stucky, *Adv. Funct. Mater.* **13**, 301 (2003).